Eur. J. Mineral., 36, 55–72, 2024
https://doi.org/10.5194/ejm-36-55-2024

European Journal of Mineralogy
Open Access

Atomic-scale environment of niobium in ore minerals as revealed by XANES and EXAFS at the Nb K-edge

Quentin Bollaert[1], Mathieu Chassé[1], Guillaume Morin[1], Benoît Baptiste[1], Alexandra Courtin[2], Laurence Galoisy[1], Gautier Landrot[3], Cécile Quantin[2], and Georges Calas[1]

[1]Institut de Minéralogie, de Physique des Matériaux et de Cosmochimie, Sorbonne Université, 4 place Jussieu, Paris, 75005, France
[2]Géosciences Paris-Saclay (GEOPS), UMR 8148 Université Paris-Saclay – CNRS, 91405 Orsay CEDEX, France
[3]Synchrotron SOLEIL, L'Orme des Merisiers, Saint-Aubin, BP 48 91192 Gif-sur-Yvette CEDEX, France

Correspondence: Quentin Bollaert (qbollaert@me.com)

Received: 5 April 2023 – Revised: 20 October 2023 – Accepted: 20 November 2023 – Published: 8 January 2024

Abstract. The mineralogy of niobium (Nb) is characterized by multicomponent oxides such as AB_2O_6, $A_2B_2O_7$, ABO_4, and ABO_3 in which Nb is incorporated in the B site. Such complex crystal-chemistry prevents their unambiguous identification in ore deposits such as hydrothermal rocks and laterites which exhibit complex and fine-grained textures. The understanding of the processes controlling Nb ore deposit formation in various geological settings is therefore limited, although Nb is a critical element. In this study, we use X-ray absorption spectroscopy (XAS) at the Nb K-edge to investigate the local atomic-scale structure around Nb in a large set of natural and synthetic minerals of geological and technological importance. Our X-ray absorption near-edge structure (XANES) data at the Nb K-edge show three major features of variable position and intensity and then can be related to the local distortion and coordination number of the Nb site. Shell-by-shell fits of the extended X-ray absorption fine structure (EXAFS) data reveal that the NbO_6 octahedra are distorted in a variety of pyrochlore species. At least two distinct first shells of O atoms are present while reported crystallographic data yield regular octahedra in the same minerals. Next-nearest Nb–Nb distances in pyrochlore and Nb-bearing perovskite mirror a corner-sharing NbO_6 network, whereas the two Nb–Nb distances in columbite are typical of edge- and corner-sharing NbO_6 octahedra. Such a resolution on the Nb site geometry and the intersite relationships between the next-nearest NbO_6 octahedra is made possible by collecting EXAFS data under optimal conditions at 20 K and up to 16 $Å^{-1}$. The local structure around substituted Nb^{5+} in Fe^{3+}, Ti^{4+}, and Ce^{4+} oxides suffers major changes relative to the unsubstituted structures. The substitution of Nb^{5+} for Ti^{4+} in anatase leads to the increase in the interatomic distances between Nb and its first and second Ti^{4+} neighbors. The substitution of Nb^{5+} for Ce^{4+} in cerianite reduces the coordination number of the cation from eight to four, and the Nb–O bonds are shortened compared to Ce–O ones. In hematite, Nb^{5+} occupies a regular site, whereas the Fe^{3+} site is strongly distorted suggesting major site relaxation due to charge mismatch. The sensitivity of XANES and EXAFS spectroscopies at the Nb K-edge to the local site geometry and next-nearest neighbors demonstrated in this study would help decipher Nb speciation and investigate mineralogical reactions of Nb minerals in deposit-related contexts such as hydrothermal and lateritic deposits.

Published by Copernicus Publications on behalf of the European mineralogical societies DMG, SEM, SIMP & SFMC.

1 Introduction

Niobium (Nb) is an uncommon 4d transition element moderately enriched in the upper continental crust relative to the solar system abundances (ca. 12 ppm vs. 1.44 ppm in CI chondrites; Rudnick and Gao, 2014). Niobium enrichment is associated with the formation of carbonatitic or alkaline–peralkaline granitic melt with bulk contents typically reaching 300–400 ppm and leading to the crystallization of Nb minerals (Chakhmouradian, 2006). Such unusual melts result from the combination of multiple fluid-related events including partial melting, fractional crystallization, liquid immiscibility, or hydrothermal remobilization (Yong et al., 2022). Deciphering the existence and relative contribution of each of these processes to Nb enrichment remains challenging (Williams-Jones and Vasyukova, 2022).

Minerals from the pyrochlore supergroup ($A_2B_2X_6Y$) are the most abundant ore minerals used for Nb production. This critical metal is essential to the manufacture of high-strength low-alloy steel (HSLA) and vacuum-graded superalloy (Silveira and Resende, 2020). Weathering-resistant pyrochlore concentrated in Brazilian laterites represents 91 % of the global Nb production with only two active mines. As the demand is expected to increase by $6\,\%\,yr^{-1}$ until 2030 (Alves and Coutinho, 2015), diversification of Nb sources is needed to ensure its supply (Omar and Veiga, 2021). Current exploration projects focus on pyrochlore ores from carbonatite (Elk Creek, Mrima Hill, Panda Hill) and alkaline granitic (Kanyika) complexes. Other minerals such as metasomatic fersmite [$(Ca,Ce,Na)(Nb,Ta,Ti)_2(O,OH,F)_6$] may be economically viable in the Aley carbonatite (Chakhmouradian et al., 2015). Small strategic deposits, such as the columbite placers in French Guiana, could also secure a country's national supply (Gourcerol et al., 2020). Additional Nb sourcing could arise from by-products of active mines including columbite-group minerals [$(Fe,Mn)Nb_2O_6$] (Bastos Neto et al., 2009), aeschynite-group minerals [$(Ce,Ca,Th)(Nb,Ti)_2O_6$] (Smith et al., 2015), and loparite–lueshite solid solution series [$(Na,REE)(Ti,Nb)_2O_6$–$NaNbO_3$] (Kogarko et al., 2002). All these phases exhibit complex crystal chemistries with cation vacancies, anion substitutions (hydroxyl groups, chlorine, fluorine), and water incorporation leading to a wide range of compositions (Mitchell, 2015). These minerals may be differentiated based on chemical characterization techniques only in pegmatites (Ercit, 2005), but identification remains equivocal in hydrothermal and supergene deposits because the typical grain size of Nb minerals is often smaller than the probe of microscopic conventional techniques (Bollaert et al., 2023a, b). The use of diffraction techniques is also complicated by frequent metamictization (Ewing, 1975). Yet, unequivocal determination of Nb mineral species is required to track the geological and geochemical genesis of Nb deposits (Liu et al., 2020) and estimate the economic viability of potential Nb deposits (Mitchell, 2015).

Due to their interesting physico-chemical properties, Nb-bearing phases are also of interest to the industry, in particular to implement low-carbon technologies. Ideal pyrochlore-type materials are considered as a superstructure of fluorite with eight atoms in the unit cell with a structure similar to natural pyrochlore (Subramanian et al., 1983). The high ionic and electric conductivity of pyrochlore result from their high flexibility and anion mobility, which are useful for solid oxide fuel cells, hydrogen production, and catalytic application (Anantharaman and Dasari, 2021). Perovskite-related phases, including Nb-bearing perovskite [$(Na,REE,Ca,Sr,Th)(Ti,Nb)O_3$], which consist of a cubic close-packed structure with corner-shared oxygen octahedra linked in three dimensions, have major applications in electroceramics (Bhalla et al., 2000). High oxide conduction in these structures is achieved by the formation of oxygen vacancies created through the partial substitution of low-valent cation for the sixfold-coordinated B site cation (Nb, Ti) (Gouget et al., 2019). Sodium niobate ($NaNbO_3$) remains one of the most enigmatic perovskite-like structure with several temperature-dependent polymorphs, and the structure of its natural analogue (lueshite) remains debated (Mitchell et al., 2018). Materials such as CeO_2, TiO_2, and Fe_2O_3 have a wide range of applications including electrode for solid oxide fuel cells (Heinzmann et al., 2016; Ma et al., 2020), photocatalysts (Chong et al., 2010), and water splitting for hydrogen production (Ashraf et al., 2020), respectively. The doping of such materials with cations such as Nb^{5+} can enhance their physico-chemical properties with respect to their undoped counterparts (Batoo et al., 2021; Siriya et al., 2022). Since the improved properties of these oxides arise from charge unbalancing, interstitial oxygen, or vacancies induced by the incorporation of Nb^{5+} in the crystal lattice, the determination of the local environment of Nb in these materials would help rationalize the origin of their enhanced physico-chemical properties.

So far, Nb K-edge X-ray absorption near-edge structure (XANES) and extended X-ray absorption fine structure (EXAFS) spectroscopies have been used to determine the local structure of Nb in synthetic oxides (Yoshida et al., 1992; Froideval et al., 2008; Haverkamp et al., 2022) and to determine the redox state of Nb in reducing conditions (Cartier et al., 2015). Only a few studies used this technique to decipher the local structure around the Nb^{5+} ion in crystalline (Piilonen et al., 2006) and metamict minerals (Nakai et al., 1987; Greegor et al., 1988). Here, we report a systematic analysis of the Nb K-edge XANES and EXAFS spectra in order to decipher the local atomic environment around Nb in ore minerals and in Nb-doped compounds where Nb local structure is unknown.

2 Materials

A set of 18 Nb compounds (Table 1), representative of Nb mineralization types, mineral groups, and industrial materials, was selected in order to study the local structural environment of this element at the atomic-scale using X-ray absorption spectroscopy at the Nb K-edge.

2.1 Natural niobium reference minerals

The selected natural compounds are oxides and silicates in which Nb^{5+} occurs in sixfold coordination except for fergusonite-(Y) and Nb-doped cerianite, in which Nb^{5+} is expected to occur in fourfold and eightfold coordination, respectively. The names given to pyrochlore samples follow IMA nomenclature scheme based on the dominant valence rule (Atencio, 2021). The prefixes "U-rich" and "Ba-rich" were added to characterize oxynatropyrochlore and kenopyrochlore samples, respectively, for petrogenetic purposes (Bhattacharjee et al., 2022). The possibilities of names for zero-valent-dominant pyrochlore (dominated by vacancies or H_2O at both A and Y sites) such as that from Lueshe (Congo) are multiple in IMA's classification. In this study, Lueshe's pyrochlore is named "hydropyrochlore". Nonetheless, due to the uncertainties concerning the dominance of H_2O/OH over vacancies, it could also be hydrokenopyrochlore or hydroxykenopyrochlore. Structural details from available crystal structure data are given in Table 1.

2.2 Synthetic niobium-doped reference minerals

Since anatase, rutile, hematite, goethite, and cerianite can concentrate Nb, but macroscopic individual Nb-bearing crystals are rarely found in natural contexts, these minerals were synthesized with Nb concentrations representative of natural enrichment, i.e., within the 1 wt % to 10 wt % Nb range. In these minerals, Nb^{5+} is expected to substitute for cations such as Ti^{4+} (rutile and anatase), Fe^{3+} (hematite and goethite), and Ce^{4+} (cerianite). These cations are sixfold coordinated except for Ce^{4+}, which is eightfold-coordinated in cerianite. The procedures of these syntheses are described in detail in Bollaert et al. (2023c). X-ray diffraction patterns of the synthetic samples do not show the presence of mineral impurities (Fig. S1 in the Supplement), suggesting that Nb was incorporated in the structure of the targeted mineral phases. The local structure around Nb was further studied by EXAFS spectroscopy as detailed hereafter.

3 Data collection and analysis

3.1 X-ray absorption spectroscopy (XAS)

3.1.1 Data collection

Nb K-edge XAS scans were collected over the 18 700 to 20 000 eV energy range on the SAMBA beamline at SOLEIL (Orsay, France) (Fonda et al., 2012) and BM23 beamline (Mathon et al., 2015) at European Synchrotron Radiation Facility (ESRF; Grenoble, France). The XANES region corresponds to about the first 50 eV above the energy of the edge (ca. 18 990–19 040 eV). A Nb foil was used to calibrate the data in energy.

Seventeen of the 18 selected samples were analyzed on the SAMBA beamline. It is equipped with a Si(220) monochromator providing a 2×0.5 mm ($H \times V$) monochromatic beam with an energy resolution of ca. 2.5 eV at 19 000 eV, i.e., better than the large core-hole lifetime of 4.14 eV (Krause and Oliver, 1979). The samples were analyzed at 20 K in a liquid He cryostat to limit thermal dampening of EXAFS oscillations. Each scan was obtained in 170 s and featured 1625 data points with a ca. 0.8 eV step. The spectrum of fergusonite-(Y) was collected in transmission mode on the BM23 beamline at room temperature. Scans of 430 data points with a ca. 4.8 eV step were acquired.

Multiple scans were collected for each sample until no significant improvement in the signal-to-noise ratio was observed. Two to six scans were collected in transmission mode for the natural Nb-rich samples (> 5 wt %). Spectra were collected on cellulose-diluted pellets in order to optimize the absorption length to ca. 2 and the edge jump to ca 1.5. Up to 30 scans were collected in fluorescence mode for the Nb-doped synthetic reference compounds containing 1 wt % Nb.

3.1.2 Data analysis

Data were merged, normalized, and background subtracted using the Larch package (Newville and Ravel, 2020). The E_0 value was fixed to 18 993 eV, which corresponds to the maximum of the first derivative of μ (E) of the Nb K-edge XANES spectra. EXAFS data were background subtracted using a cubic spline function with rbkg parameter set to the default value of 1. The normalized EXAFS oscillations were k^3-weighted and fast-Fourier-transformed (FFT) from k space to R space to obtain a radial distribution function (RDF) around central Nb atoms. Before FFT calculation, a Kaiser–Bessel window with a Bessel weight (dk) of 2 was applied over the 2.5–16 $Å^{-1}$ k range for most natural Nb-rich compounds. FFT was calculated over the 2.5–12 $Å^{-1}$ range for the Th-bearing natural compounds because of the Th L_3-edge at ca. 19 690 eV. A range of 2.5–13 $Å^{-1}$ was applied on the Nb-doped hematite due to low Nb content (ca. 1 wt %).

In order to examine the local environment around the central absorber (Nb) and the interatomic distances to its next-

Table 1. Structural and chemical information on the studied Nb compounds. The M–O distances (Å) correspond to Nb–O bonds except for aeschynite (Ti–O distances) and for Nb-doped Ti, Fe and Ce oxides (Ti–O, Fe–O and Ce–O distances). The distortion index (DI) is calculated as defined by Baur (1974). Lueshite, Nb perovskite, wöhlerite, columbite-(Mn), niocalite samples were provided by École Nationale Supérieure des Mines de Paris (ENSMP). Fergusonite-(Y), fluorcalciopyrochlore, hydropyrochlore, Ba-rich kenopyrochlore, and aeschynite-(Y) were provided by the mineral collection of Sorbonne Université (SU). Uranium-rich oxynatropyrochlore sample is a fragment of sample number 214 (HU 1024503) studied in Lumpkin and Ewing (1995).

Minerals	Location of the studied sample	Ideal formula	Expected structure from previous studies	Reported M–O range (Å)	Reported DI (%)	Reference
$^{[4]}$Nb-bearing references						
Fergusonite-(Y)	Malaysia	$YNbO_4$	Isolated NbO_4 tetrahedra sharing edges with YO_8 polyhedra	1.802–1.813	0.3	Guastoni et al. (2010)
$^{[6]}$Nb-bearing references						
U-rich oxynatropyrochlore	Woodcox mine, USA	(Na, Ca, U)$_2$Nb$_2$O$_6$O	Completely metamict	–	–	Lumpkin and Ewing (1995)
Fluorcalciopyrochlore	Tatarka, Russia	(Ca,Na)$_2$Nb$_2$O$_6$F	Corner-sharing NbO_6 octahedra sharing edges with A-site cation	1.90, 1.92, 1.93, 1.94 depending on the crystal	0.0	Perrault (1968)
Hydropyrochlore	Lueshe, Congo	(H$_2$O,□)Nb$_2$(O,OH)$_6$(H$_2$O)	Corner-sharing NbO_6 octahedra sharing edges with A-site cation	1.986	0.0	Ercit et al. (1994)
Ba-rich kenopyrochlore	Bingo, Congo	(□,Ba)Nb$_2$O$_6$	Corner-sharing NbO_6 octahedra sharing edges with A-site cation	1.970	0.0	Groult et al. (1975)
Lueshite	Lueshe, Congo	$NaNbO_3$	Perovskite structure with interconnected NbO_6 octahedra with interstitial Na	1.970–1.981	0.2	Mitchell et al. (2018)
Niobium perovskite	Oka, Canada	$CaTi_{1-2x}Fe_xNb_xO_3$	Perovskite structure with interconnected NbO_6 octahedra with interstitial Ca	1.972–2.005	0.6	Chakhmouradian and Mitchell (1998)
Aeschynite-(Y)	Iveland, Norway	(Y,Ln,Ca,Th)(Ti,Nb)$_2$(O,OH)$_6$	Corner- and edge-sharing NbO_6	1.876–2.146	3.7	Bonazzi and Menchetti (1999)
Wöhlerite	Telemark, Norway	Na$_2$Ca$_4$ZrNb(Si$_2$O$_7$)$_2$O$_3$F	Isolated NbO_6 octahedra sharing corners and edges with SiO_4, ZrO_6, NaO_7, CaO_8	1.911–2.274	5.2	Mellini and Merlino (1979)
Columbite-(Mn)	Musha, Rwanda	(Mn,Fe)(Nb,Ta)$_2$O$_6$	Chains of edge-sharing NbO_6 octahedra	1.800–2.281	6.0	Wenger et al. (1991)
Niocalite	Oka, Canada	Ca$_7$Nb(Si$_4$O$_{14}$)O$_3$F	Isolated NbO_6 octahedra sharing edges and corners with CaO_6 octahedra	1.885–2.259	6.1	Mellini (1982)

Table 1. Continued.

Minerals	Location of the studied sample	Ideal formula	Expected structure from previous studies	Reported M–O range (Å)	Reported DI (%)	Reference
$^{[6]}$Nb synthetic samples						
Rutile (5 wt % Nb)		TiO_2	Edge- and corner-sharing TiO_6 octahedra (two edges are shared with each other)	1.947–1.982	0.6	Meagher and Lager (1979)
Anatase (1 wt % Nb, 5 wt % Nb, 10 wt % Nb)		TiO_2	Edge-sharing TiO_6 octahedra (four edges are shared with each other)	1.934–1.980	1.0	Horn et al. (1972)
Goethite (1 wt % Nb)		α-FeOOH	Chains of edge-sharing FeO_6 octahedra joined by corner-sharing FeO_6	1.933–2.106	3.8	Yang et al. (2006)
Hematite (1 wt % Nb)		α-Fe_2O_3	Face- and edge-sharing FeO_6 octahedra	1.946–2.116	4.2	Blake (1965)
$^{[8]}$Nb synthetic samples						
Cerianite (1 wt % Nb)		CeO_2	Edge-sharing CeO_8 polyhedra	2.343	0.0	Zaitsev et al. (2011)

nearest neighbor atoms, shell-by-shell fitting of the Nb K-edge EXAFS data was performed in k space using backscattering phase and amplitude functions generated by the FEFF 8 code. Fit quality was estimated by a reduced χ^2_R of the following form:

$$\chi^2_R = \frac{N_{\text{idp}}}{N_{\text{points}}(N_{\text{idp}} - N_{\text{p}})} \frac{1}{\epsilon^2} \Sigma[k^3\chi_{\text{exp}}(k) - k^3\chi_{\text{calc}}(k)]^2, \quad (1)$$

where $N_{\text{idp}} = (2\Delta k \Delta R)/\pi)$ is the number of independent parameters, N_{p} is the number of free fit parameters, N_{points} is the number of data points, and ε is the estimated quadratic average of the data noise (Newville and Ravel, 2020). For the Nb minerals, phase shift and amplitude functions were extracted using the FEFF 8 code based on reported crystallographic data (Table 1). For Nb-doped compounds, the phase shift and amplitude functions of the examined paths were obtained by substituting the central atoms (Fe, Ti, Ce) for Nb. Depending on the shape of the FFT, the first two, three, or four single-scattering paths were taken into account in the fitting procedure. Fit parameters include the interatomic distances (R, in Å), a Debye–Waller factor (σ^2, in Å^2), which is a measure of the effects of structural and vibrational disorder on the EXAFS signal, the difference between the theoretical threshold energy and experimentally determined threshold energy (ΔE_0, in eV). Coordination number around the absorber was fixed to the expected value for most minerals of known structure (except for fluorcalciopyrochlore sample), but this parameter was fitted for Nb-doped oxides (Nb-substituted hematite, cerianite, anatase, and rutile) of unknown local environment. The amplitude reduction factor S_0^2 was fixed to 1. Estimates of the uncertainties on the fitted parameters are made according to the standard statistical treatment of experimental data (Bevington and Robinson, 1992; Newville and Ravel, 2020). Such derived uncertainties reflect the uncertainties and correlations between variables.

3.2 Electron probe microanalyses (EPMA)

Electron probe microanalysis (EPMA) was performed on a CAMECA SXFive EPMA equipped with five wavelength-dispersive spectrometers (WDSs) at the Centre d'Analyse des Minéraux de Paris (CAMPARIS). An accelerating potential of 15 kV and a sample current of 40 nA for major elements and 299 nA for minor ones were used to analyze the chemical composition of the natural samples. Niobium content was determined using the L lines. Wavelength-dispersive spectroscopy analyses were performed using the following standards: albite for Na; diopside for Mg, Si, and Ca; orthoclase for Al and K; $MnTiO_3$ for Mn and Ti; hematite for Fe; $BaSO_4$ for Ba; topaz for F; $LiNbO_3$ for Nb; metallic Ta for Ta; SrSi for Sr; zircon for Zr; galena for Pb; monazite for Th; uraninite for U; and allanite-(Y) for Y, La, Ce, and Nd. The crystal-chemical composition and the crystallographic data of the geological references can be found in Tables S1–S3 (Supplement).

3.3 Single-crystal X-ray diffraction (XRD)

A single crystal of hydropyrochlore was mounted on a Kapton loop, and the diffraction data were recorded at the X-ray diffraction platform of the IMPMC with an Oxford Diffraction (Rigaku) Xcalibur S four-circle diffractometer using MoK_{alpha} wavelength. The diffractometer is equipped with a graphite monochromator and a Sapphire CCD detector. The data were processed with the CrysAlisPro software (CrysAlisPro 1.171.38.41, Rigaku Oxford Diffraction, 2015).

The structure was solved with Shelxt (Sheldrick, 2015). The stoichiometry was attributed according to elemental analysis using EPMA analysis. Further attempts to freely refine the occupancies of some sites were unsuccessful or led to correlations and bad results. The structure was refined by a full-matrix least-square method on structure factors with Shelxl-2014 (Sheldrick, 2015) using the Olex2 interface (Dolomanov et al., 2009). Further details regarding the data collection and structure refinements are given in Tables S4–S8.

4 Results and discussion

4.1 Relationship between niobium site geometry and K-edge XANES spectroscopic properties

Three distinct features are observed in the Nb K-edge XANES spectra of the studied compounds (Fig. 1): a pre-edge feature (A) at ca. 18 983 eV, a B feature at ca. 18 999 eV, and a C feature at ca. 19 012 eV. The pre-edge feature was fitted (Fig. 2) using a pseudo-Voigt, combined with a Gaussian function to account for the baseline (Wilke et al., 2005). Best results were obtained using pseudo-Voigts with a Lorentzian to Gaussian component of 0.99 (Fig. 2). By analogy with 3d elements, the pre-edge feature of 4d elements results from weakly quadrupole-allowed $1s \rightarrow 4d$ transition (Farges, 1996; Laplaza et al., 1996). Upon breaking centrosymmetry, 5p–4d hybridization has a dramatic influence on the intensity of the pre-edge feature by allowing dipolar $1s \rightarrow 5p$–4d transitions (Getty et al., 2008).

The intensity and energy of the pre-edge vary from 0.16–0.31 over the 18 982–18 985.5 eV energy range (Table 2). Pre-edge features in pyrochlore spectra are of lower intensity (0.20–0.23) and located at higher energy (18 983–18 984 eV) than most other Nb minerals spectra, indicating a lower degree of distortion of the Nb site (Yamamoto, 2008). However, the pre-edge feature of U-rich oxynatropyrochlore spectrum is more intense (0.26) and located at higher energy (19 985 eV) than the other pre-edges of pyrochlore spectra (Table 2). This increase in the pre-edge feature has been related to the loss of site symmetry due to radiation damage (Greegor et al., 1988). Spectra of Nb minerals with the most intense pre-edge features (0.24–0.26) such as wöhlerite, columbite (Fig. 2b), and niocalite are those of the compounds with the highest degree of Nb site distortion. Despite the weak distortion of Nb sites in Nb perovskite (Fig. 2a), the fit of the pre-edge of Nb perovskite spectrum reveals the contribution of a small shoulder that may be assigned to charge transfer between the 4d orbitals of Nb^{5+} and the 2p orbitals of O^{2-} (Bollaert et al., 2023c), which may enhance the transition momentum of the electric dipole transition (Westre et al., 1997). The pre-edge feature in the Nb-doped cerianite spectrum stands out by its sharp and intense pre-edge (0.31) at low energy (18 982.6 eV) (Table 2). Such an intense pre-edge feature may reflect the breaking of centrosymmetry of the eight-fold site upon Nb^{5+} for Ce^{4+} substitution. We note that the pre-edge feature in Nb-doped anatase spectrum (Table 2) with 10 wt % Nb is more intense (0.250) than those with 1 % and 5 % Nb (0.220). This difference indicates an increasing distortion of the local structure with increasing amounts of Nb in the anatase structure, which is corroborated by the increase of the unit-cell parameters (Fig. S1).

The position and intensity of the B feature, which is assigned to a $1s \rightarrow 4p$ transition, are subject to variations in the 18 997–19 004 eV range (Fig. 1a). The B feature in the columbite and lueshite spectra is split into two poorly resolved features including a low-intensity shoulder at 19 004 eV, which has been used to show the high degree of distortion of NbO_6 octahedra in columbite (Piilonen et al., 2006). The high-energy position of the B feature in lueshite spectrum (19 003 eV) can be related to multiple scattering paths involving second-nearest neighbors as inferred from Zr K-edge spectra (Farges and Rossano, 2000). In the spectrum of Nb-doped cerianite, the B feature is split into two well-marked B_1 and B_2 features (at 18 998 and 19 006 eV, respectively).

The energy position of the C feature varies from 19 010 to 19 022 eV among the spectra of natural Nb minerals (Fig. 1) reflecting the wide range of variation in Nb–O distances. The XANES spectra of columbite, wöhlerite, and niocalite with a low-energy C feature (ca. 19 010 eV) are also those with the longest Nb–O distances, whereas minerals with the shortest Nb–O distances like pyrochlores exhibit a shift of the C spectral feature towards higher energies (Table 1). This correlation between the position of the C feature and the bond distance between the absorber and the first scatterer has been evidenced not only in different transition elements such as Cr, Mn, V, and Ti (Bianconi et al., 1985) but also for the same absorbing atom in different minerals (Farges and Rossano, 2000). All the visible features (Fig. 1a) above the B feature may arise from a transition to higher-energy *np* states, shape resonance, and multiple scattering (Wong et al., 1984; Borg et al., 2012).

The XANES spectrum of Nb perovskite also displays the most intense C feature (Fig. 1), which is consistent with a limited distortion of the NbO_6 octahedra (Farges and Rossano, 2000). Apart from the C feature, the well-defined features of low intensity especially visible in the spectrum of Nb perovskite (but also in the lueshite spectrum) occur-

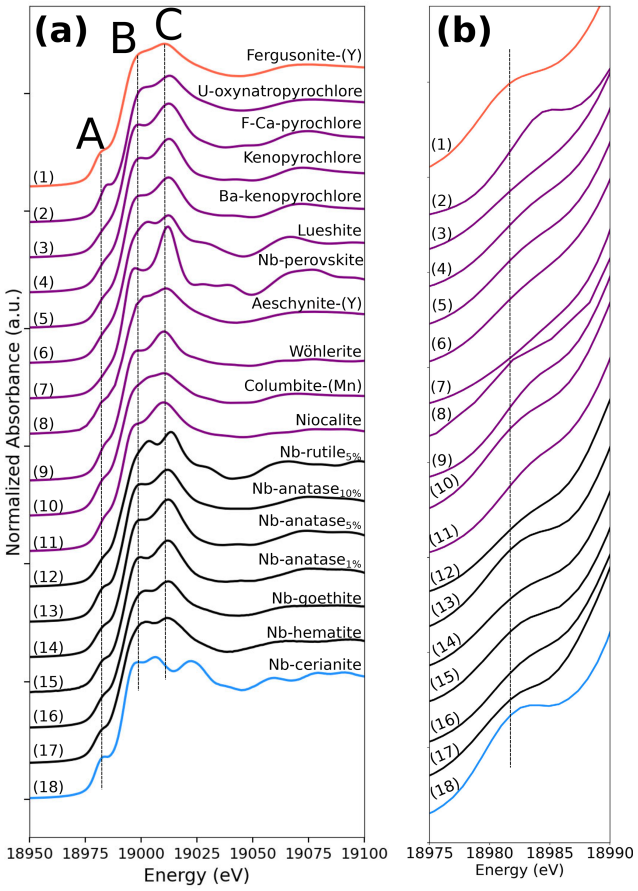

Figure 1. Niobium K-edge XANES spectra of the range of compounds studied. **(a)** XANES region and **(b)** close-up on the pre-edge feature. Niobium is present as Nb^{5+} ion in sixfold coordination in all phases analyzed except for Nb-doped cerianite (18) and fergusonite-(Y) (1) in which Nb^{5+} is expected to be eightfold- and fourfold-coordinated, respectively. The vertical lines are aligned on the features of fergusonite-(Y) for comparative purposes.

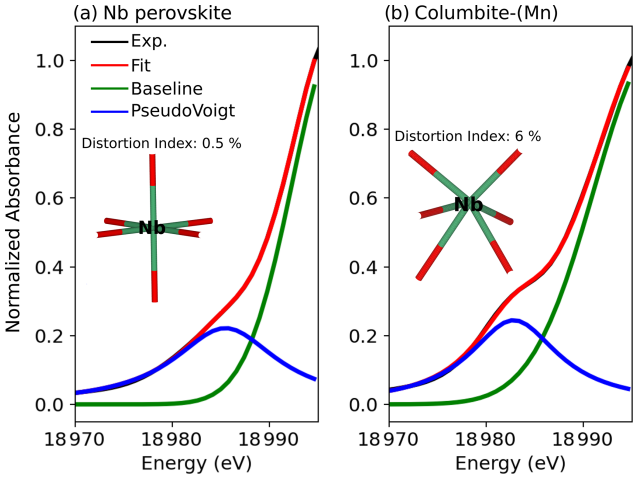

Figure 2. Pre-edge analysis of the Nb K-edge of **(a)** Nb perovskite and **(b)** columbite-(Mn) evidencing the sensitivity of the pre-edge to the Nb site geometry. The black and red spectra correspond to experimental (Exp.) and fitted data (Fit.), respectively. The blue line represents the pre-edge feature fitted with one pseudo-Voigt (the fitted relative weight of Lorentzian to Gaussian component is 0.99 in all samples). The green line corresponds to a fitted Gaussian background (Wilke et al., 2005).

ring a few tens of electronvolts after the edge jump (Fig. 1) correspond to multiple scattering, which may involve strong ordering of the next-nearest-neighbor atoms (Mountjoy et al., 2000).

The spectra of fergusonite-(Y) and aeschynite-(Y) exhibit broad and weak C features, similar to the spectrum of U-rich oxynatropyrochlore, which may indicate a broad distribution of Nb–O bond lengths and the loss of long-range periodicity. This similarity as well as their intense pre-edge features (0.229 and 0.250) may reflect the metamictization of aeschynite-(Y) and fergusonite-(Y) structures, common in these radionuclide-rich phases (Ewing, 1975).

4.2 Revisiting the local structure of niobium in pyrochlore through EXAFS spectroscopy

The differences evidenced in the XANES spectra of pyrochlores reflect distinct Nb local environments that can be confirmed by shell-by-shell fitting analysis of the EXAFS data. The FFT spectra of pyrochlore (Fig. 3) exhibit two contributions in the 1–2 Å range (uncorrected for phase shift). The fit of the fluorcalciopyrochlore spectra using the crystal structure of Perrault (1968) (Fig. S2), in which Nb^{5+} occupies regular octahedra, does not reproduce the second FFT peak at ca. 1.7–2.0 Å (uncorrected phase shift). To obtain consistent fits to the data (χ^2_R = ca. 0.4, Fig. 3a), it is necessary to take into account for two Nb–O paths (2.0 O_1 at 1.91 Å and 4.0 O_2 at 2.06 Å). Even though fluorcalciopyrochlore is one of the most common species of pyrochlore (Nasraoui et al., 1999; Thompson et al., 2002), only one recent study has investigated the structure of fluorcalciopyrochlore with X-ray powder diffraction, reporting a regular Nb site with a single coordination shell at 2.00 Å (Guowu et al., 2016). Crystallographic data on fluorine-calcium-enriched pyrochlore also yield a regular NbO_6 site but with different Nb–O distances: 1.90–1.95 (Perrault, 1968) and 1.97 Å (Bonazzi, 2006). The only Nb K-edge EXAFS data on a natural pyrochlore sample show only the first-neighbor contribution in the FFT spectrum (Piilonen et al., 2006), although the chemical composition and the XANES spectra of this fluorcalciopyrochlore are similar to our data. This difference may result from the quality of our EXAFS data which were collected at 20 K and up to 16 $Å^{-1}$, which enhances EXAFS data accuracy.

In comparison with fluorcalciopyrochlore, the first-neighbor contribution for hydropyrochlore and Ba-rich kenopyrochlore display an increase in intensity of the long Nb–O contribution (Fig. 3b, c), with two short Nb–

Table 2. Summary of the parameters obtained from the pre-edge fitting analysis. The data are presented in order of increasing pre-edge intensity.

Sample	Intensity (a.u.)	Energy (eV)	Area (a.u.)	Full width at half maximum (eV)	$1000 \cdot \chi^2$
Rutile 5 % Nb	0.163	18 982.71	3.16	12.32	14.73
Fluorcalciopyrochlore	0.200	18 983.93	4.01	12.76	4.50
Lueshite	0.203	18 983.71	3.94	12.37	5.04
Ba-rich kenopyrochlore	0.214	18 983.67	3.99	11.86	5.03
Hematite	0.215	18 982.14	3.77	11.16	10.71
Goethite	0.216	18 983.17	3.90	11.46	8.85
Anatase 5 % Nb	0.218	18 982.90	3.88	10.84	2.68
Anatase 1 % Nb	0.220	19 882.78	3.63	10.50	3.21
Nb perovskite	0.221	18 985.45	4.51	12.95	2.57
Hydropyrochlore	0.226	18 984.00	4.16	11.72	4.33
Aeschynite-(Y)	0.229	18 982.79	3.79	10.57	1.62
Niocalite	0.240	18 983.95	4.21	11.13	6.20
Columbite-(Mn)	0.245	18 982.83	4.31	11.20	7.42
Fergusonite-(Y)	0.250	18982.24	3.99	10.17	13.45
Anatase 10 % Nb	0.250	18 982.85	4.43	10.09	2.82
Wöhlerite	0.258	18 984.08	4.84	13.40	14.45
U-rich oxynatropyrochlore	0.260	18 985.0	4.00	9.57	1.81
Cerianite	0.306	18 982.58	4.88	9.33	12.28

O bonds (1.89 and 1.91 Å) and four longer Nb–O bonds (2.09 and 2.09 Å). The XRD-derived structures of zero-valent-dominant pyrochlore indicate variable Nb–O distances (1.96–2.00 Å) depending on the crystal chemistry of the species (Biagioni et al., 2018; Li et al., 2020; Agakhanov et al., 2021; Miyawaki et al., 2021), but none of these studies identified a distortion of the Nb octahedra. We refined the structure of the studied hydropyrochlore sample using single-crystal X-ray diffraction data (Tables S3–S7). The refined crystal structure (Fd-3m, $a = 10.59$ Å and Nb–O = 1.98 Å), consistent with other published data (Ercit et al., 1994), does not indicate any distortion of NbO_6 octahedra. The difference between the local structure around Nb in hydropyrochlore derived from EXAFS and XRD data results from the intrinsic differences between these techniques. EXAFS spectroscopy is sensitive to local geometry around the absorbing atom, whereas X-ray diffraction detects long-range periodicity and yields an average crystal structure that may overlook local distortion (Giuli et al., 2001, 2012). Studies using XAS and pair distribution function (PDF) from neutron total scattering on synthetic pyrochlores with a wide range of chemical composition show that the structure of pyrochlores can be more complex than that obtained from X-ray diffraction. In these studies, the distortion of the B site is shown to increase with the size of the A-site cation (Zhang et al., 2013; Blanchard et al., 2013; Shamblin et al., 2016). The differences of Nb local structures between our study and recent studies of geological samples of pyrochlores using XRD (Biagioni et al., 2018; Li et al., 2020; Agakhanov et al., 2021; Miyawaki et al., 2021) mirror the sensitivity of XANES and EXAFS to Nb site distortion. The present study provides the first evidence of a distortion of Nb site in natural pyrochlore.

Our fits show that the EXAFS contribution to the third FFT peaks at 3–4 Å (uncorrected for phase shift in Fig. 3) of fluorcalciopyrochlore, hydropyrochore, and Ba-rich kenopyrochlore arises from six Nb second neighbors at a Nb–Nb distance ranging from 3.61 to 3.72 Å (Table 3). These distances characterize corner-sharing octahedra, in agreement with the structure of pyrochlore (Fig. 5).

The fit of metamict U-rich oxynatropyrochlore spectrum (Fig. 3d) indicates Nb–O distances (1.97 and 2.11 Å) similar to those of other crystalline pyrochlores (Table 3). However, Nb^{5+} is $(5+1)$-fold oxygen coordinated, which differs from the $(4+2)$-fold coordination found in hydropyrochlore and Ba-rich kenopyrochlore. The effect of metamictization has been described as leading to a decrease in coordination number and interatomic distances for structures such as zircon (Farges and Calas, 1991) or euxenite (Greegor et al., 1984). In this study, the effect of metamictization on the first Nb–O shell is weak, as also observed for various metamict pyrochlores (Greegor et al., 1988). In zircon, the Zr polyhedra are edge-sharing, while in pyrochlore, Nb octahedra are connected by corners. This structural difference may account for the different sensitivity to metamictization of zircon and pyrochlore structures. In the studied metamict pyrochlore sample, the second-neighbor contributions to the EXAFS data are of particularly low intensity and are fitted by considering only 1.3 Nb–Nb at 3.51 Å (Table 3). This latter distance is reduced from 4 % to 6 % with respect to Nb–Nb distances found in the other studied pyrochlore samples (Ta-

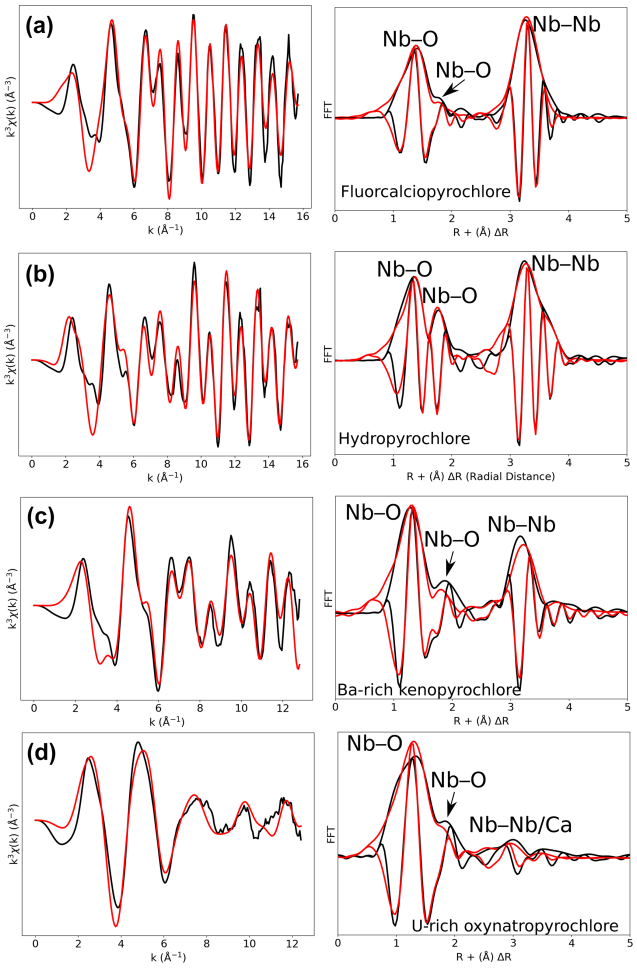

Figure 3. Results of shell-by-shell fits of Nb K-edge EXAFS data for **(a)** fluorcalciopyrochlore, **(b)** hydropyrochlore, **(c)** Ba-rich kenopyrochlore, and **(d)** U-rich oxynatropyrochlore. The k^3-weighted EXAFS spectra were fit in k space as shown in the left panels, and fast Fourier transforms (FFT) are plotted in the right panels. Experimental and fitted curves are displayed as black and red lines, respectively.

ble 3). Adding a Nb–Ca contribution with 0.8 Ca (12 wt % CaO in U-rich oxynatropyrochlore, Table S1) improves the quality of the fit. The low intensity of the Nb–Nb and Nb–Ca contributions results from disrupted periodicity increasing the local disorder around Nb (Greegor et al., 1988).

4.3 Characterizing the local environment of niobium in Nb ore minerals

4.3.1 Columbite-(Mn)

In columbite, the local environment of Nb consists in a strongly distorted octahedron (Table 4), which is consistent with crystal structure data (Wenger et al., 1991; Tarantino, 2005) that yield 6.0 distinct Nb–O distances (1.80, 1.92, 1.96, 2.06, 2.07, and 2.28 Å). Our data, collected up to a k value of 16 $Å^{-1}$ and at 20 K, allow determining the Nb–O distances with greater accuracy than previous EXAFS studies (Piilonen et al., 2006) that showed only a single average Nb–O distance (2.03 Å). Two Nb–Nb distances are obtained (3.30 and 3.59 Å) (Table 4) reflecting corner- and edge-sharing Nb octahedra (Fig. 5), present in the structure of columbite (Chukanov et al., 2023). The sensitivity of EXAFS data could therefore be used to track changes in Nb site geometry and in intersite relationships between Nb octahedra occurring during the columbitization of pyrochlore, a reaction that occurs in hydrothermal contexts (Tremblay et al., 2017; Wu et al., 2021).

4.3.2 Perovskite-group minerals: Nb perovskite and lueshite

The geometry of the first O shell determined by EXAFS in Nb perovskite (1.97 Å, Table 4) is consistent with the crystal structure refinement of $CaTi_{0.8}Fe_{0.1}Nb_{0.1}O_3$ (Chakhmouradian and Mitchell, 1998, who reported 4.0 Nb–O distances at 1.96 Å and 2.0 at 1.98 Å). EXAFS analysis of lueshite shows two shells of oxygen neighbors at 1.94 and 2.14 Å (Fig. 4c and Table 4), indicating an elongation of NbO_6 octahedra. In the structure of lueshite, Nb occupies three crystallographically distinct NbO_6 octahedra (Mitchell et al., 2018). The two Nb–O distances obtained from EXAFS data may reflect average contributions of a distribution of Nb–O distances resulting from the presence of three sites, a weakly distorted octahedron (1.974–1.982 Å), and two more distorted ones (1.953–2.078 and 1.895–2.019 Å). However, the largest Nb–O distances are more important in the studied lueshite than in the latter crystal structure. The identification of Nb-bearing perovskite is made difficult by the existence of numerous solid solutions between end-member compositions ($Ca_2Nb_2O_7$, $Ca_2Fe^{3+}NbO_6$, $CaTiO_3$, and $NaNbO_3$) (Mitchell et al., 2017). As the XAS signatures of lueshite and Nb perovskite are distinct (Fig. 1), the use of Nb K-edge XANES and EXAFS spectroscopies may help differentiate perovskites from each other in rock samples, in particular in undersaturated rocks such as kimberlite, carbonatite, and nepheline syenites, which host various Nb-bearing perovskites (Mitchell and Kjarsgaard, 2002).

4.4 Local environment of substituted niobium in Ti, Ce, and Fe oxides

4.4.1 Niobium-doped Ti oxides

The average Nb–O distances (1.97 Å) are larger than the Ti–O distances in pure anatase (1.94 Å), which is consistent with the larger ionic radius of $^{VI}Nb^{5+}$ (0.64 Å) compared to $^{VI}Ti^{4+}$ (0.605 Å). Similarly to the Ti site in pure anatase, the Nb site may be slightly distorted, but the distances are too close to be distinguished using EXAFS. Our study gives interatomic distances consistent with the literature (Table 6).

Table 3. Results of the shell-by-shell fits of EXAFS data for the pyrochlore samples. R_{calc} (Å): calculated interatomic distances; R_{ref} (Å): expected interatomic distance from XRD crystal structure data; N: number of neighbors; σ^2: Debye–Waller factor; ΔE_0 (eV): difference between the user-defined threshold energy and the experimentally determined threshold energy, in electronvolts. The amplitude reduction factor S_0^2 was fixed to 1. Fit quality is estimated by a χ^2 value, and uncertainties in reported parameters are given within brackets.

Sample	R_{calc} (Å)	R_{ref} (Å)	N	σ (Å^2)	ΔE_0 (eV)	χ^2_R
Fluorcalciopyrochlore	1.91 (±0.01)	1.941	2.0 Nb–O	0.004 (±0.0005)	−9 (±2)	0.37
	2.06 (±0.02)	/	4.0 Nb–O	0.002 (±0.001)	–	
	3.70 (±0.009)	3.675	6.0 Nb–Nb	0.005 (±0.0002)	–	
Hydropyrochlore	1.89 (±0.01)	1.972	2.0 Nb–O	0.002 (±0.002)	−1 (±2)	0.44
	2.09 (±0.02)	/	4.0 Nb–O	0.009 (±0.007)	–	
	3.72 (±0.01)	3.684	6.0 Nb–Nb	0.005 (±0.0006)	–	
Ba-rich kenopyrochlore	1.91 (±0.01)	1.970	2.0 Nb–O	0.006 (±0.0006)	−8 (±1)	1.05
	2.09 (±0.01)	/	4.0 Nb–O	0.004 (±0.001)	–	
	3.61 (±0.02)	3.750	6.0 Nb–Nb	0.013 (±0.003)	–	
U-rich oxynatropyrochlore	1.97 (±0.02)	2.00	5.0 Nb–O	0.013 (±0.004)	−2 (±2)	0.28
	2.11 (±0.02)	/	1.0 Nb–O	0.004 (±0.001)	–	
	3.51 (±0.05)	3.67	1.3 Nb–Nb	0.010 (±0.020)	–	
	3.55 (±0.05)	3.67	0.8 Nb–Ca	0.002 (±0.010)	–	

Table 4. Results of the shell-by-shell fits of EXAFS data for columbite-(Mn), Nb perovskite, and lueshite. R_{calc} (Å): calculated interatomic distances; R_{ref} (Å): expected interatomic distance from XRD crystal structure data; N: number of neighbors; σ^2: Debye–Waller factor; ΔE_0 (eV): difference between the user-defined threshold energy and the experimentally determined threshold energy, in electronvolts. The amplitude reduction factor S_0^2 was fixed to 1. Fit quality is estimated by a χ^2 value, and uncertainties in reported parameters are given within brackets.

Sample	R_{calc} (Å)	R_{ref} (Å)	N	σ (Å^2)	ΔE_0 (eV)	χ^2_R
Columbite-(Mn)	1.87 (±0.009)		2.0 Nb–O	0.003 (±0.0007)	−3 (±1)	0.76
	2.02 (±0.01)	1.80–2.28	2.0 Nb–O	0.0006 (±0.001)	–	
	2.18 (±0.02)		2.0 Nb–O	0.001 (±0.002)	–	
	3.30 (±0.01)	3.27	2.0 Nb–Nb	0.010 (±0.001)	–	
	3.59 (±0.02)	3.52	2.0 Nb–Mn	0.007 (±0.003)	–	
	3.70 (±0.02)	3.66	2.0 Nb–Nb	0.004 (±0.0005)	–	
Lueshite	1.94 (±0.01)	1.97–1.98	4.0 Nb–O	0.007 (±0.001)	+0 (±2)	1.07
	2.14 (±0.02)		2.0 Nb–O	0.002 (±0.001)	–	
	3.32 (±0.03)	3.35	4.0 Nb–Na	0.006 (±0.005)	–	
	3.46 (±0.03)	3.42	4.0 Nb–Na	0.005 (±0.005)	–	
	4.03 (±0.02)	3.91	4.0 Nb–Nb	0.009 (±0.001)	–	
Nb perovskite	1.97 (±0.006)	1.97–2.00	6.0 Nb–O	0.005 (±0.0003)	−6 (±2)	0.57
	3.31 (±0.01)	3.19–3.37	3.6 (±3.1) Nb–Ca	0.011 (±0.008)	–	
	3.86 (±0.03)	3.86	6.0 Nb–Nb	0.012 (±0.002)	–	

Depending on the amount of substituted Nb, the methods of synthesis, and the quality of the data, the increase in first cation–oxygen distances resulting from Nb substitution is in the range of +0.005 to +0.05 Å with respect to pure anatase (Table 6). The Nb–Ti distances at 3.12 and 3.87 Å (Table 5) are representative of edge- and corner-sharing octahedra, respectively (Fig. 7). The substitution of Nb for Ti influences the medium-range structure as probed by the increase of the Nb–Ti distances relatively to Ti–Ti distances by +0.08 and +0.10 Å (Table 5). This may result from stronger Coulombic repulsion of Nb–Ti with respect to Ti–Ti. The first oxygen shell is less affected by this effect since the greater attraction of Nb^{5+} is compensated by its larger ionic radius (Marchiori et al., 2014).

A single Nb–O path (Fig. 6b) was found to be suitable to fit the EXAFS data of Nb-doped rutile (2.00 Å), thus confirming the weakly distorted Nb site probed by the pre-edge feature (Fig. 1b) as expected from the symmetry of the Ti site in pure rutile (Howard et al., 1991). We however show that the substitution of Ti^{4+} for Nb^{5+} in rutile induces an

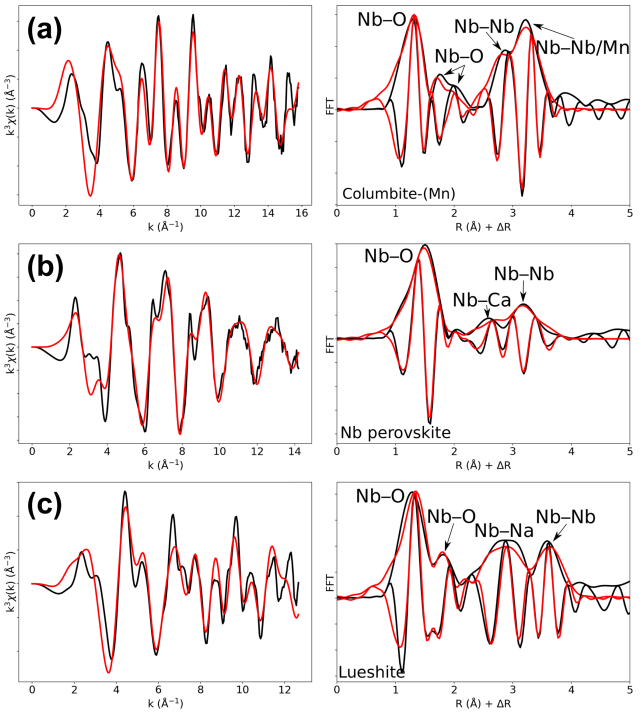

Figure 4. Results of shell-by-shell fits of Nb K-edge EXAFS data for **(a)** columbite-(Mn), **(b)** Nb perovskite, and **(c)** lueshite. The k^3-weighted EXAFS spectra were fit in k space as shown in the left panels, and fast Fourier transforms are plotted in the right panels. Experimental and fitted curves are displayed as black and red lines, respectively.

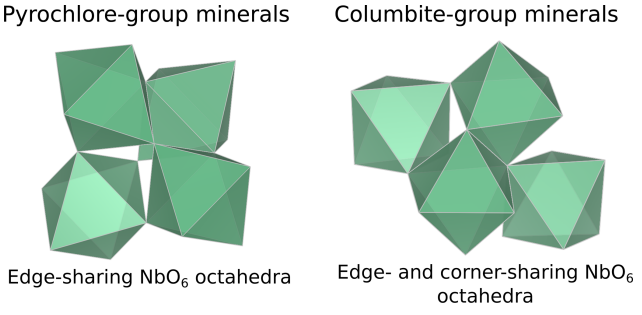

Figure 5. General view of the intersite relationships between NbO_6 octahedra in the pyrochlore-group (Bonazzi, 2006) and columbite-group (Wenger et al., 1991) minerals.

enlargement of the first oxygen shell by +0.05 Å (Table 5). In Nb-doped rutile, two shells of Ti at 3.07 and 3.65 Å (Table 5) yield a good fit (Fig. 6b). Although the substitution has an effect on the medium-range structure by increasing the Nb–Ti distances relative to Ti–Ti distances (Table 5), the intersite relationships between the octahedra seem preserved since the two Nb–Ti distances match characteristic edge- and corner-sharing Ti sites in rutile (Fig. 7).

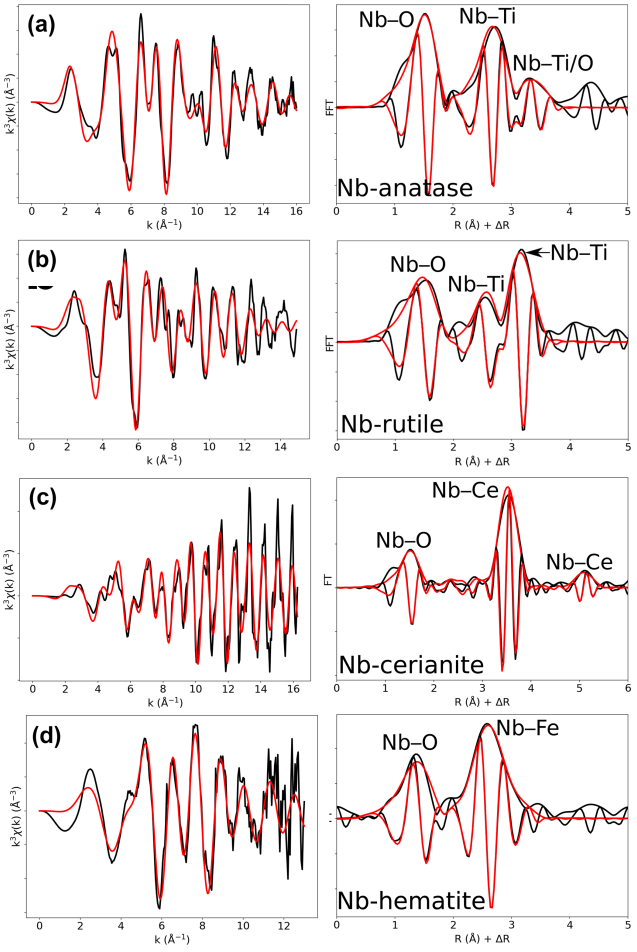

Figure 6. Results of shell-by-shell fits of Nb K-edge EXAFS data for **(a)** Nb-doped anatase, **(b)** Nb-doped rutile, **(c)** Nb-doped cerianite, and **(d)** Nb-doped hematite. The k^3-weighted EXAFS spectra were fit in k space as shown in the left panels, and fast Fourier transforms are plotted in the right panels. Experimental and fitted curves are displayed as black and red lines, respectively.

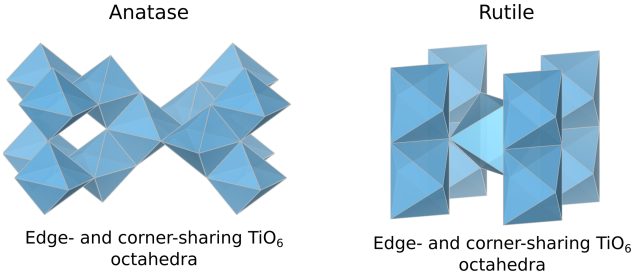

Figure 7. General view of the intersite relationships between TiO_6 octahedra in anatase (Horn et al., 1972) and rutile (Meagher and Lager, 1979).

Table 5. Results of the shell-by-shell fits of EXAFS data for Nb-doped reference materials. R_{calc} (Å): calculated interatomic distances; R_{ref} (Å): expected interatomic distance from XRD crystal structure data; N: number of neighbors; σ^2: Debye–Waller factor; ΔE_0 (eV): difference between the user-defined threshold energy and the experimentally determined threshold energy, in electronvolts; χ^2: goodness of fit. The amplitude reduction factor S_0^2 was fixed to 1. Fit quality is estimated by a χ^2 value, and uncertainties in reported parameters are given within brackets.

Sample	R_{calc} (Å)	R_{ref} (Å)	N	σ (Å^2)	ΔE_0 (eV)	χ^2_R
Nb-anatase (5 %)	1.97 (±0.007)	1.934–1.980	5.7 (±0.8) Nb–O	0.006 (±0.001)	−7 (±2)	0.14
	3.12 (±0.008)	3.04	4.0 Nb–Ti	0.005 (±0.0004)	–	
	3.87 (±0.08)	3.86	8.0 Nb–O	0.006 (±0.005)	–	
	3.89 (±0.07)	3.78	4.0 Nb–Ti	0.012 (±0.006)	–	
Nb-rutile (5 %)	2.00 (±0.009)	1.947–1.982	6.0 (±1.2) Nb–O	0.011 (±0.002)	0 (±1)	2.16
	3.07 (±0.011)	2.96	2.0 Nb–Ti	0.006 (±0.001)	–	
	3.65 (±0.007)	3.57	8.0 Nb–Ti	0.007 (±0.0004)	–	
Nb-cerianite (1 %)	1.95 (±0.009)	2.34	4.0 Nb–O	0.004 (±0.0008)	−2 (±1)	0.27
	2.93 (±0.03)	2.34	4.0 Nb–O	0.007 (±0.004)	–	
	3.83 (±0.005)	3.83	12.0 Nb–Ce	0.004 (±0.0004)	–	
	5.41 (±0.01)	5.42	6.0 Nb–Ce	0.005 (±0.001)	–	
Nb-hematite (1 %)	1.92 (±0.01)	1.946–2.116	3.3 (±0.8) Nb–O	0.010 (±0.003)	−5 (±1)	0.22
	3.04 (±0.01)	2.97	3.0 Nb–Fe	0.0006 (±0.001)	–	
	3.46 (±0.03)	3.36	3.0 Nb–Fe	0.010 (±0.002)	–	

Table 6. Comparison of Nb–O and Nb–Ti interatomic distances as a function of the degree of Nb enrichment in anatase.

Nb enrichment of anatase (wt % Nb)	Bonds	R (Å)	N	σ (Å^2)	ΔE_0 (eV)	Ref
1	Nb–O	1947	6	12	5.8	Bouchet et al. (2003)
	Nb–Ti_1	3112	4	15		
	Nb–Ti_2	3951	4	27		
3	Nb–O	1.99	6	3	?	Bhachu et al. (2014)
	Nb–Ti_1	3.11	4	5		
	Nb–Ti_2	3.92	4	5		
7	Nb–O	1.98	6	1	?	Gardecka et al. (2015)
	Nb–Ti_1	3.13	4	4		
	Nb–Ti_2	3.85	4	7		
5	Nb–O	1.97	5.7	6	−7	This study
	Nb–Ti_1	3.12	4	5		
	Nb–O	3.87	8	6		
	Nb–Ti_2	3.89	4	12		
Pure anatase	Ti–O	1.94	6	14		Knauth et al. (2009)
	Ti–Ti_1	3.04	4	12		
	Ti–Ti_2	3.79	4	25		
	Ti–O	3.8	8	17		

4.4.2 Nb-doped cerianite

The first oxygen shell of Nb-doped cerianite exhibits only one Nb–O distance of 1.95 Å (Table 5). The fitted coordination number for this Nb–O path is 4.0 (Table 5), whereas Ce is eightfold-coordinated in CeO_2 (Zaitsev et al., 2011). Ab initio calculations indicate that Nb substitution in cerianite splits the oxygen shell into two fourfold shells (Muhich and Steinfeld, 2017; Kolodiazhnyi et al., 2019). A first shell of short Nb–O bond distances is associated with a shift of Nb toward the face center of the cube, as observed for Fe^{3+} in cerianite (Ma et al., 2020). In addition, Nb is also bonded to the four remaining oxygens forming longer dangling bonds (Nb–O = 2.93 Å, Table 5).

The similar position and high intensity of the pre-edge (ca. 19 982 eV) of fourfold-coordinated fergusonite-(Y) and Nb-doped cerianite (Fig. 1b) may also be indicative of the strong contribution of the first fourfold shell. The similarity of their pre-edge features cannot be related to the presence of fergusonite-(Ce) formed during the synthesis of cerianite (Kolodiazhnyi et al., 2016) given the absence of impurities on the corresponding XRD pattern (Fig. S1). The peak of large intensity in the FFT (Fig. 6c) corresponds to a shell of 12 Ce atoms ($R_{Nb–Ce} = 3.83$ Å) as expected for pure cerianite. This distance indicates that there is no relaxation at medium-range during Nb–Ce substitution (Table 5).

4.4.3 Nb-doped hematite

In contrast to the highly distorted Fe site in hematite with interatomic distances ranging from 1.95 to 2.12 Å (Blake, 1965), EXAFS data analysis (Fig. 6d) indicates a single oxygen shell with a Nb–O distance of 1.92 Å (Table 5). Charge balance may be maintained by substituting $5Fe^{3+}$ for $3Nb^{5+}$, which have similar ionic radii (0.645 and 0.64 Å for $^{VI}Fe^{3+}$ and $^{VI}Nb^{5+}$, respectively), coupled to the formation of cation vacancies (Oliveira et al., 2008; Melgarejo et al., 2012). This structural readjustment may induce some local relaxation resulting in the symmetrization of the Nb site and the formation of regular NbO_6 octahedra (Bollaert et al., 2023c). The high Debye–Waller factors may mirror a dispersion in distances, centered around 1.92 Å (Table 5), due to the crystal defects resulting from the incorporation of Nb^{5+} in the crystal lattice of hematite.

The face-, edge-, and corner-sharing Fe sites correspond to the broad second contribution, fitted by two shells of three Fe atoms at a distance of 3.04 and 3.46 Å from the central Nb absorbing atom (Table 5). The incorporation of Nb^{5+} in hematite significantly modifies the interatomic distances of Nb–Fe shells relative to Fe–Fe in pure hematite (Table 5). As is the case with anatase, this could result from stronger Coulombic repulsion of Nb–Fe with respect to Fe–Fe.

The symmetrization of the octahedra also occurs for Sb sites in Sb-doped hematite (Mitsunobu et al., 2013). Since Sb^{5+} has the same charge and an ionic radius close to Nb^{5+} ($^{VI}Sb^{5+} = 0.60$ Å), the substitution of Sb^{5+} for Fe^{3+} in hematite is likely governed by the same charge compensation mechanism leading to similar structural changes. Conversely, the incorporation of highly charged cations such as U^{6+} ($^{VI}U^{6+} = 0.73$ Å) and Mo^{6+} ($^{VI}Mo^{6+} = 0.59$ Å) with larger differences of ionic radii compared to Fe^{3+} results in a distorted octahedral site because of the distinct mechanisms of substitution involved ($2Fe^{3+}$ for Mo^{6+}) (Kerisit et al., 2016; Görn et al., 2021).

5 Conclusion

This study provides the first comprehensive analysis of Nb K-edge XANES and EXAFS spectra in a large data set of the most common natural Nb minerals and Nb-based oxides used in industry. We highlight the relationship between Nb site geometry and K-edge XANES spectroscopic properties by showing the influence of Nb site distortion on the intensity of the pre-edge feature. The features after the edge-jump display notable differences, reflecting average Nb–O distances, medium-range ordering and metamictization. Ab initio theoretical investigation would be required to fully understand the variations in the features. EXAFS data complement the pre-edge feature evidence by probing the Nb site geometry and the intersite relationships with the next-nearest neighbors. Shell-by-shell fits of the EXAFS data reveal the distortion of the Nb octahedra in various pyrochlores, which cannot be detected through X-ray diffraction. The calculation of the next-nearest Nb atoms in common Nb ore minerals mirrors the intersite relationships between edge- and corner-sharing NbO_6 octahedra in columbite and corner-sharing NbO_6 octahedra only in pyrochlore and Nb-bearing perovskite. The degree of accuracy of the interatomic distances in this study results from the optimal conditions of EXAFS data acquisition (at 20 K, with a reliable signal-to-noise ratio up to 16 $Å^{-1}$). The effect of the Nb incorporation into oxides depends on the substituted cations and on the host structure. In anatase, the substitution of Nb^{5+} for Ti^{4+} leads to an increase in the interatomic distances of the first and second neighbors. In cerianite, the substitution of Nb^{5+} for Ce^{4+} reduces the coordination of the cation site from an eightfold to a fourfold site. In hematite, the substitution of Nb^{5+} for Fe^{3+} induces vacancies, allowing a symmetrization of the Nb site by relaxation of the structure. These results are useful as they prove the efficiency of XAS at the Nb K-edge to study the unknown atomic-scale environment of Nb resulting from the substitution for other cations in technological materials. As these Nb-substituted oxides are also found in alteration contexts, this technique could help rationalize the affinity of Nb for these different phases in hydrothermal and lateritic contexts. With this study, we show the potential of Nb K-edge XANES and EXAFS spectroscopies when combined with conventional mineralogical techniques to decipher Nb speciation and investigate chemical reactions of Nb minerals in deposit-related contexts such as hydrothermal and lateritic deposits.

Data availability. All raw data derived from this research are found in the following Zenodo depository: https://doi.org/10.5281/zenodo.7801896 (Bollaert et al., 2023d).

Supplement. The supplement related to this article is available online at: https://doi.org/10.5194/ejm-36-55-2024-supplement.

Author contributions. QB collected EPMA, XRD, and XAS data; analyzed and interpreted the data; and wrote the initial manuscript. MC collected XAS data, participated in the interpretation of the data, and contributed to the writing of the manuscript. GM supervised shell-by-shell fit of EXAFS spectra, contributed to the presentation of EXAFS data, and participated in the writing. BB performed XRD structure refinement. AC and CQ participated to XAS data acquisition and commented on the manuscript. XAS data collection was conducted under the supervision of GL. LG and GC participated in guiding the research and contributed to the writing of the manuscript.

Competing interests. The contact author has declared that none of the authors has any competing interests.

Disclaimer. Publisher's note: Copernicus Publications remains neutral with regard to jurisdictional claims made in the text, published maps, institutional affiliations, or any other geographical representation in this paper. While Copernicus Publications makes every effort to include appropriate place names, the final responsibility lies with the authors.

Special issue statement. This article is part of the special issue "Probing the Earth: spectroscopic methods applied to mineralogy". It is not associated with a conference.

Acknowledgements. We thank the curators of the mineralogical collections of MINES ParisTech and Sorbonne University: Eloïse Gaillou, Jean-Claude Bouillard, and Paola Giura, for providing the natural samples of Nb minerals. We are grateful to Peter C. Burns and Ginger E. Sigmon for providing the metamict pyrochlore sample (U-rich oxynatropyrochlore: sample 214). We thank Michel Fialin and Nicolas Rividi for their assistance in acquiring microprobe data. We acknowledge SOLEIL for providing beam time, and the staff of the SAMBA (proposal no. 20200363) beamline is thanked for their assistance during beam time. We acknowledge the European Synchrotron Radiation Facility (ESRF) for provision of synchrotron radiation facilities, and we would like to thank Olivier Mathon for the collection of fergusonite-(Y) spectra on BM23 beamline.

Review statement. This paper was edited by Francesco Di Benedetto and reviewed by Gabriele Giuli and one anonymous referee.

References

Agakhanov, A. A., Kasatkin, A. V., Britvin, S. N., Siidra, O. I., Pautov, L. A., Pekov, I. V., and Karpenko, V. Y.: Cesiokenopyrochlore, the First Natural Niobate with an Inverse Pyrochlore Structure, Can. Mineral., 59, 149–157, https://doi.org/10.3749/canmin.2000056, 2021.

Alves, A. R. and Coutinho, A. D. R.: The Evolution of the Niobium Production in Brazil, Mat. Res., 18, 106–112, https://doi.org/10.1590/1516-1439.276414, 2015.

Anantharaman, A. P. and Dasari, H. P.: Potential of pyrochlore structure materials in solid oxide fuel cell applications, Ceram. Int., 47, 4367–4388, https://doi.org/10.1016/j.ceramint.2020.10.012, 2021.

Ashraf, M., Khan, I., Usman, M., Khan, A., Shah, S. S., Khan, A. Z., Saeed, K., Yaseen, M., Ehsan, M. F., Tahir, M. N., and Ullah, N.: Hematite and Magnetite Nanostructures for Green and Sustainable Energy Harnessing and Environmental Pollution Control: A Review, Chem. Res. Toxicol., 33, 1292–1311, https://doi.org/10.1021/acs.chemrestox.9b00308, 2020.

Atencio, D.: Pyrochlore-Supergroup Minerals Nomenclature: An Update, Front. Chem., 9, 713368, https://doi.org/10.3389/fchem.2021.713368, 2021.

Bastos Neto, A. C., Pereira, V. P., Ronchi, L. H., de Lima, E. F., and Frantz, J. C.: The world-class Sn, Nb, Ta, F (Y, REE, Li) deposit and the massive cryolite associated with the albite-enriched facies of the madeira A-type granite, Pitinga Mining District, Amazonas state, Brazil, Can. Mineral., 47, 1329–1357, https://doi.org/10.3749/canmin.47.6.1329, 2009.

Batoo, K. M., Verma, R., Chauhan, A., Kumar, R., Hadi, M., Aldossary, O. M., and Al-Douri, Y.: Improved room temperature dielectric properties of Gd^{3+} and Nb^{5+} co-doped Barium Titanate ceramics, J. Alloy. Compd., 883, 160836, https://doi.org/10.1016/j.jallcom.2021.160836, 2021.

Baur, W. H.: The geometry of polyhedral distortions. Predictive relationships for the phosphate group, Acta Crystallogr. B, 30, 1195–1215, https://doi.org/10.1107/S0567740874004560, 1974.

Bevington, P. R. and Robinson, D. K.: Data reduction and Error Analysis for the Physical Sciences, 2nd Edn., McGraw-Hill, New York, 328 pp., 1992.

Bhachu, D. S., Sathasivam, S., Sankar, G., Scanlon, D. O., Cibin, G., Carmalt, C. J., Parkin, I. P., Watson, G. W., Bawaked, S. M., Obaid, A. Y., Al-Thabaiti, S., and Basahel, S. N.: Solution Processing Route to Multifunctional Titania Thin Films: Highly Conductive and Photcatalytically Active $Nb:TiO_2$, Adv. Funct. Mater., 24, 5075–5085, https://doi.org/10.1002/adfm.201400338, 2014.

Bhalla, A. S., Guo, R., and Roy, R.: The perovskite structure – a review of its role in ceramic science and technology, Mater. Res. Innov., 4, 3–26, https://doi.org/10.1007/s100190000062, 2000.

Bhattacharjee, S., Dey, M., Chakrabarty, A., Mitchell, R. H., and Ren, M.: Zero-Valent-Dominant Pyrochlores: Endmember Formula Calculation and Petrogenetic Significance, Can. Mineral., 60, 469–484, https://doi.org/10.3749/canmin.2100058, 2022.

Biagioni, C., Meisser, N., Nestola, F., Pasero, M., Robyr, M., Roth, P., Schnyder, C., and Gieré, R.: Hydrokenopyrochlore, $(\square,\#)_2Nb_2O_6\cdot H_2O$, a new species of the pyrochlore supergroup from the Sahatany Pegmatite Field, Antananarivo Province, Madagascar, Eur. J. Mineral., 30, 869–876, https://doi.org/10.1127/ejm/2018/0030-2761, 2018.

Bianconi, A., Fritsch, E., Calas, G., and Petiau, J.: X-ray-absorption near-edge structure of 3d transition elements in tetrahedral coordination: The effect of bond-length variation, Phys. Rev. B, 32, 4292–4295, https://doi.org/10.1103/PhysRevB.32.4292, 1985.

Blake, G. R.: Bulk Density, in: Methods of Soil Analysis, edited by: Black, C. A., 374–390, American Society of Agronomy, Madison, WI, https://doi.org/10.2134/agronmonogr9.1.c30, 1965.

Blanchard, P. E. R., Liu, S., Kennedy, B. J., Ling, C. D., Avdeev, M., Aitken, J. B., Cowie, B. C. C., and Tadich, A.: Investigating the Local Structure of Lanthanoid Hafnates $Ln_2Hf_2O_7$ via Diffraction and Spectroscopy, J. Phys. Chem. C, 117, 2266–2273, https://doi.org/10.1021/jp311329q, 2013.

Bollaert, Q., Chassé, M., Allard, T., Courtin, A., Galoisy, L., Landrot, G., Quantin, C. Vantelon, D., and Calas, G.: Multiscale processes controlling niobium mobility during supergene weathering, Geochim. Cosmochim. Ac., 353, 142–157, https://doi.org/10.1016/j.gca.2023.05.023, 2023a.

Bollaert, Q., Chassé, M., Bastos Neto, A., Baptiste, B., Courtin, A., Galoisy, L., Mathon, O., Quantin, C. Vantelon, D., and Calas, G.: Mechanisms leading to exceptional niobium concentration during lateritic weathering: The key role of secondary oxides, Chem. Geol., 641, 121767, https://doi.org/10.1016/j.chemgeo.2023.121767, 2023b.

Bollaert, Q., Chassé, M., Elnaggar, H., Juhin, A., Courtin, A., Galoisy, L., Quantin, C., Retegan, M., Vantelon, D., and Calas, G.: Niobium speciation in minerals revealed by $L_{2,3}$-edges XANES spectroscopy, Am. Mineral., 108, 595–605, https://doi.org/10.2138/am-2022-8293, 2023c.

Bollaert, Q., Chassé, M., Morin, G., Baptiste, B., Courtin, A., Galoisy, L., Landrot, G., Quantin, C., and Calas, G.: Atomic-scale environment of niobium in minerals as revealed by X-ray absorption spectroscopy at the Nb K-edge, Zenodo [data set], https://doi.org/10.5281/zenodo.7801896, 2023d.

Bonazzi, P.: Single-crystal diffraction and transmission electron microscopy studies of "silicified" pyrochlore from Narssarssuk, Julianehaab district, Greenland, Am. Mineral., 91, 794–801, https://doi.org/10.2138/am.2006.1777, 2006.

Bonazzi, P. and Menchetti, S.: Crystal chemistry of aeschynite-(Y) from the Western Alps; residual electron density on difference-Fourier map, Eur. J. Mineral., 11, 1043–1049, https://doi.org/10.1127/ejm/11/6/1043, 1999.

Borg, S., Liu, W., Etschmann, B., Tian, Y., and Brugger, J.: An XAS study of molybdenum speciation in hydrothermal chloride solutions from 25–385 °C and 600 bar, Geochim. Cosmochim. Ac., 92, 292–307, https://doi.org/10.1016/j.gca.2012.06.001, 2012.

Bouchet, R., Weibel, A., Knauth, P., Mountjoy, G., and Chadwick, A. V.: EXAFS Study of Dopant Segregation (Zn, Nb) in Nanocrystalline Anatase (TiO_2), Chem. Mater., 15, 4996–5002, https://doi.org/10.1021/cm034640n, 2003.

Cartier, C., Hammouda, T., Boyet, M., Mathon, O., Testemale, D., and Moine, B. N.: Evidence for Nb^{2+} and Ta^{3+} in silicate melts under highly reducing conditions: A XANES study, Am. Mineral., 100, 2152–2158, https://doi.org/10.2138/am-2015-5330, 2015.

Chakhmouradian, A. R.: High-field-strength elements in carbonatitic rocks: Geochemistry, crystal chemistry and significance for constraining the sources of carbonatites, Chem. Geol., 235, 138–160, https://doi.org/10.1016/j.chemgeo.2006.06.008, 2006.

Chakhmouradian, A. R. and Mitchell, R. H.: A Structural Study of the Perovskite Series $CaTi_{1-2x}Fe_xNb_xO_3$, J. Solid State Chem., 138, 272–277, https://doi.org/10.1006/jssc.1998.7803, 1998.

Chakhmouradian, A. R., Reguir, E. P., Kressall, R. D., Crozier, J., Pisiak, L. K., Sidhu, R., and Yang, P.: Carbonatite-hosted niobium deposit at Aley, northern British Columbia (Canada): Mineralogy, geochemistry and petrogenesis, Ore Geol. Rev., 64, 642–666, https://doi.org/10.1016/j.oregeorev.2014.04.020, 2015.

Chong, M. N., Jin, B., Chow, C. W. K., and Saint, C.: Recent developments in photocatalytic water treatment technology: A review, Water Res., 44, 2997–3027, https://doi.org/10.1016/j.watres.2010.02.039, 2010.

Chukanov, N. V., Pasero, M., Aksenov, S. M., Britvin, S. N., Zubkova, N. V., Yike, L., and Witzke, T.: Columbite supergroup of minerals: nomenclature and classification, Mineral. Mag., 87, 18–33, https://doi.org/10.1180/mgm.2022.105, 2023.

Dolomanov, O. V., Bourhis, L. J., Gildea, R. J., Howard, J. A. K., and Puschmann, H.: OLEX2: a complete structure solution, refinement and analysis program, J. Appl. Crystallogr., 42, 339–341, https://doi.org/10.1107/S0021889808042726, 2009.

Ercit, T. S.: Identification and Alteration Trends of Granitic-Pegmatite-Hosted (Y,REE,U,Th)(Nb,Ta,Ti) Oxide Minerals: A Statistical Approach, Can. Mineral., 43, 1291–1303, https://doi.org/10.2113/gscanmin.43.4.1291, 2005.

Ercit, T. S., Hawthorne, F. C., and Cerny, P. E. T. R.: The structural chemistry of kalipyrochlore, a "hydropyrochlore", Can. Mineral., 32, 415–420, 1994.

Ewing, R. C.: The Crystal Chemistry of Complex Niobium and Tantalum Oxides. IV. The Metamict State: Discussion, Am. Mineral., 60, 728–733, 1975.

Farges, F.: Coordination of Ti in crystalline and glassy fresnoites: A high-resolution XANES spectroscopy study at the Ti K-edge, J. Non-Cryst. Solids, 204, 53–64, https://doi.org/10.1016/0022-3093(96)00392-4, 1996.

Farges, F. and Calas, G.: Structural analysis of radiation damage in zircon and thorite: an X-ray absorption spectroscopic study, Am. Mineral., 76, 60–73, 1991.

Farges, F. and Rossano, S.: Water in Zr-bearing synthetic and natural glasses, Eur. J. Mineral., 12, 1093–1107, https://doi.org/10.1127/0935-1221/2000/0012-1093, 2000.

Fonda, E., Rochet, A., Ribbens, M., Barthe, L., Belin, S., and Briois, V.: The SAMBA quick-EXAFS monochromator: XAS with edge jumping, J. Synchrotron Radiat., 19, 417–424, https://doi.org/10.1107/S0909049512009703, 2012.

Froideval, A., Degueldre, C., Segre, C. U., Pouchon, M. A., and Grolimund, D.: Niobium speciation at the metal/oxide interface of corroded niobium-doped Zircaloys: A X-ray absorption near-edge structure study, Corros. Sci., 50, 1313–1320, https://doi.org/10.1016/j.corsci.2008.01.011, 2008.

Gardecka, A. J., Goh, G. K. L., Sankar, G., and Parkin, I. P.: On the nature of niobium substitution in niobium doped titania thin films by AACVD and its impact on electrical and optical properties, J. Mater. Chem. A, 3, 17755–17762, https://doi.org/10.1039/C5TA03772G, 2015.

Getty, K., Delgado-Jaime, M. U., and Kennepohl, P.: Assignment of pre-edge features in the Ru K-edge X-ray absorption spectra of organometallic ruthenium complexes, Inorg. Chim. Acta, 361, 1059–1065, https://doi.org/10.1016/j.ica.2007.07.029, 2008.

Giuli, G., Paris, E., Wu, Z., Brigatti, M. F., Cibin, G., Mottana, A., and Marcelli, A.: Experimental and Theoretical XANES and EXAFS study of tetra-ferriphlogopite, Eur. J. Mineral., 13, 1099–1108, https://doi.org/10.1127/0935-1221/2001/0013-1099, 2001.

Giuli, G., Cicconi, M. R., and Paris, E.: $^{[4]}Fe^{3+}$-O distance in synthetic kimzeyite garnet, $Ca_3Zr_2[Fe_2SiO_{12}]$, Eur. J. Mineral., 24, 783–790, 2012.

Görn, M. G., Bolanz, R. M., Parry, S., Göttlicher, J., Steininger, R., and Majzlan, J.: Incorporation of Mo^{6+} in ferrihydrite, goethite, and hematite, Clay. Clay Miner., 69, 188–204, https://doi.org/10.1007/s42860-021-00116-x, 2021.

Gouget, G., Duttine, M., Chung, U.-C., Fourcade, S., Mauvy, F., Braida, M.-D., Le Mercier, T., and Demourgues, A.: High Ionic Conductivity in Oxygen-Deficient Ti-Substituted Sodium Niobates and the Key Role of Structural Features, Chem. Mater., 31, 2828–2841, https://doi.org/10.1021/acs.chemmater.8b05292, 2019.

Gourcerol, B., Serrand, A.-S., Chevillard, M., and Kroonenberg, S.: Potentiel géologique du coltan en Guyane: état des lieux et perspectives sud-américaines, Géologues, 206, 49–53, 2020.

Greegor, R. B., Lytle, F. W., Ewing, R. C., and Haaker, R. F.: Ti-site Geometry in Metamict, Annealed and Synthetic Complex Ti-Nb-Ta Oxides by X-Ray Absorption Spectroscopy, Nucl. Instrum. Met.-B, 1, 587–594, 1984.

Greegor, R. B., Lytle, F. W., Chakoumakos, B. C., Lumpkin, G. R., Warner, J. K., and Ewing, R. C.: Characterization of Radiation Damage at the Nb Site in Natural Pyrochlores and Samarskites by X-Ray Absorption Spectroscopy, MRS Proc., 127, 261–268, https://doi.org/10.1557/PROC-127-261, 1988.

Groult, D., Michel, C., and Raveau, B.: Sur de nouveaux pyrochlores lacunaires d'ions bivalents synthetises par echanges d'ions, J. Radioanal. Nucl. Chem., 37, 2203–2205, https://doi.org/10.1016/0022-1902(75)80857-8, 1975.

Guastoni, A., Cámara, F., and Nestola, F.: Arsenic-rich fergusonite-beta-(Y) from Mount Cervandone (Western Alps, Italy): Crystal structure and genetic implications, Am. Mineral., 95, 487–494, 2010.

Guowu, L., Guangming, Y., Fude, L., Ming, X., Xiangkun, G., Baoming, P., and de Fourestier, J.: Fluorcalciopyrochlore, A New Mineral Species From Bayan Obo, Inner Mongolia, P.R. China, Can. Mineral., 54, 1285–1291, https://doi.org/10.3749/canmin.1500042, 2016.

Haverkamp, R. G., Kappen, P., Sizeland, K. H., and Wallwork, K. S.: Niobium K-Edge X-ray Absorption Spectroscopy of Doped TiO_2 Produced from Ilmenite Digested in Hydrochloric Acid, ACS Omega, 7, 28258–28264, https://doi.org/10.1021/acsomega.2c02676, 2022.

Heinzmann, R., Issac, I., Eufinger, J.-P., Ulbrich, G., Lerch, M., Janek, J., and Indris, S.: Observing Local Oxygen Interstitial Diffusion in Donor-Doped Ceria by ^{17}O NMR Relaxometry, J. Phys. Chem. C, 120, 8568–8577, https://doi.org/10.1021/acs.jpcc.6b03341, 2016.

Horn, M., Schwebdtfeger, C. F., and Meagher, E. P.: Refinement of the structure of anatase at several temperatures, Z. Kristallogr., 136, 273–281, 1972.

Howard, C. J., Sabine, T. M., and Dickson, F.: Structural and thermal parameters for rutile and anatase, Acta Crystallogr. B, 47, 462–468, https://doi.org/10.1107/S010876819100335X, 1991.

Kerisit, S., Bylaska, E. J., Massey, M. S., McBriarty, M. E., and Ilton, E. S.: Ab Initio Molecular Dynamics of Uranium Incorporated in Goethite (α-FeOOH): Interpretation of X-ray Absorption Spectroscopy of Trace Polyvalent Metals, Inorg. Chem., 55, 11736–11746, https://doi.org/10.1021/acs.inorgchem.6b01773, 2016.

Knauth, P., Chadwick, A. V., Lippens, P. E., and Auer, G.: EXAFS Study of Dopant Ions with Different Charges in Nanocrystalline Anatase: Evidence for Space-Charge Segregation of Acceptor Ions, Chem. Phys. Chem., 10, 1238–1246, https://doi.org/10.1002/cphc.200800806, 2009.

Kogarko, L. N., Williams, C. T., and Woolley, A. R.: Chemical evolution and petrogenetic implications of loparite in the layered, agpaitic Lovozero complex, Kola Peninsula, Russia, Mineral. Petrol., 74, 1–24, https://doi.org/10.1007/s710-002-8213-2, 2002.

Kolodiazhnyi, T., Sakurai, H., Belik, A. A., and Gornostaeva, O. V.: Unusual lattice evolution and magnetochemistry of Nb doped CeO_2, Acta Mater., 113, 116–123, https://doi.org/10.1016/j.actamat.2016.04.052, 2016.

Kolodiazhnyi, T., Tipsawat, P., Charoonsuk, T., Kongnok, T., Jungthawan, S., Suthirakun, S., Vittayakorn, N., and Maensiri, S.: Disentangling small-polaron and Anderson-localization effects in ceria: Combined experimental and first-principles study, Phys. Rev. B, 99, 035144, https://doi.org/10.1103/PhysRevB.99.035144, 2019.

Krause, M. O. and Oliver, J. H.: Natural widths of atomic K and L levels, K α X-ray lines and several K L L Auger lines, J. Phys. Chem. Ref. Data, 8, 329–338, https://doi.org/10.1063/1.555595, 1979.

Laplaza, C. E., Johnson, M. J. A., Peters, J. C., Odom, A. L., Kim, E., Cummins, C. C., George, G. N., and Pickering, I. J.: Dinitrogen Cleavage by Three-Coordinate Molybdenum(III) Complexes: Mechanistic and Structural Data, J. Am. Chem. Soc., 118, 8623–8638, https://doi.org/10.1021/ja960574x, 1996.

Li, T., Li, Z., Fan, G., Fan, H., Zhong, J., Jahdali, N. S., Qin, M., Jehani, A. M., Wang, F., and Nahdi, M. M.: Hydroxyplumbopyrochlore, $(Pb_{1.5},\square_{0.5})Nb_2O_6(OH)$, a new member of the pyrochlore group from Jabal Sayid, Saudi Arabia, Mineral. Mag., 84, 785–790, https://doi.org/10.1180/mgm.2020.69, 2020.

Liu, S., Ding, L., Fan, H.-R., Yang, K.-F., Tang, Y.-W., She, H.-D., and Hao, M.: Hydrothermal genesis of Nb mineralization in the giant Bayan Obo REE-Nb-Fe deposit (China): Implicated by petrography and geochemistry of Nb-bearing minerals, Precambrian Res., 348, 105864, https://doi.org/10.1016/j.precamres.2020.105864, 2020.

Lumpkin, G. R. and Ewing, R. C.: Geochemical alteration of pyrochlore group minerals; pyrochlore subgroup, Am. Mineral., 80, 732–743, https://doi.org/10.2138/am-1995-7-810, 1995.

Ma, Y., Ma, Y., Giuli, G., Euchner, H., Gross, A., Lepore, G. O., d'Acapito, F., Geiger, D., Biskupek, J., Kaiser, U., Schutz, H. M., Carlsson, A., Diemant, T., Behm, R. J., Kuenzel, M., Passerini, S., and Bresser, D.: Introducing highly redox-active atomic centers in insertion-type electrodes for Lithium Ion Batteries, Adv. Energy Mater., 10, 2000783, https://doi.org/10.1002/aenm.202000783, 2020.

Marchiori, C., Di Liberto, G., Soliveri, G., Loconte, L., Lo Presti, L., Meroni, D., Ceotto, M., Oliva, C., Cappelli, S., Cappelletti, G., Aieta, C., and Ardizzone, S.: Unraveling the Cooperative Mechanism of Visible-Light Absorption in Bulk N,Nb Codoped TiO_2 Powders of Nanomaterials, J. Phys. Chem. C, 118, 24152–24164, https://doi.org/10.1021/jp507143z, 2014.

Mathon, O., Beteva, A., Borrel, J., Bugnazet, D., Gatla, S., Hino, R., Kantor, I., Mairs, T., Munoz, M., Pasternak, S., Perrin, F., and Pascarelli, S.: The time-resolved and extreme conditions XAS (TEXAS) facility at the European Synchrotron Radiation Facility: the general-purpose EXAFS bending-magnet beamline BM23, J. Synchrotron Radiat., 22, 1548–1554, https://doi.org/10.1107/S1600577515017786, 2015.

Meagher, E. P. and Lager, G. A.: Polyhedral thermal expansion in the TiO_2 polymorphs; refinement of the crystal structures of rutile and brookite at high temperature, Can. Mineral., 17, 77–85, 1979.

Melgarejo, J. C., Costanzo, A., Bambi, A. C. J. M., Gonçalves, A. O., and Neto, A. B.: Subsolidus processes as a key factor on the distribution of Nb species in plutonic carbonatites: The Tchivira case, Angola, Lithos, 152, 187–201, https://doi.org/10.1016/j.lithos.2012.06.024, 2012.

Mellini, M.: Niocalite revised: twinning and crystal structure, Tscher. Miner. Petrog., 30, 249–266, 1982.

Mellini, M. and Merlino, S.: Refinement of the crystal structure of wöhlerite, Mineral. Petr., 26, 109–123, https://doi.org/10.1007/BF01081296, 1979.

Mitchell, R. H.: Primary and secondary niobium mineral deposits associated with carbonatites, Ore Geol. Rev., 64, 626–641, https://doi.org/10.1016/j.oregeorev.2014.03.010, 2015.

Mitchell, R. H. and Kjarsgaard, B. A.: Solubility of niobium in the system $CaCO_3$–$Ca(OH)_2NaNbO_3$ at 0.1 GPa pressure, Contrib. Mineral. Petr., 144, 93–97, https://doi.org/10.1007/s00410-002-0384-3, 2002.

Mitchell, R. H., Welch, M. D., and Chakhmouradian, A. R.: Nomenclature of the perovskite supergroup: A hierarchical system of classification based on crystal structure and composition, Mineral. Mag., 81, 411–461, https://doi.org/10.1180/minmag.2016.080.156, 2017.

Mitchell, R. H., Kennedy, B. J., and Knight, K. S.: The crystal structure of lueshite at 298 K resolved by high-resolution time-of-flight neutron powder diffraction, Phys. Chem. Miner., 45, 77–83, https://doi.org/10.1007/s00269-017-0905-2, 2018.

Mitsunobu, S., Muramatsu, C., Watanabe, K., and Sakata, M.: Behavior of Antimony(V) during the Transformation of Ferrihydrite and Its Environmental Implications, Environ. Sci. Technol., 47, 9660–9667, https://doi.org/10.1021/es4010398, 2013.

Miyawaki, R., Momma, K., Matsubara, S., Sano, T., Shigeoka, M., and Horiuchi, H.: Hydroxykenopyrochlore, $(\square,Ce,Ba)_2(Nb,Ti)_2O_6(OH,F)$, a new member of the pyrochlore group from Araxá, Minas Gerais, Brazil, Can. Mineral., 59, 589–601, https://doi.org/10.3749/canmin.2000094, 2021.

Mountjoy, G., Anderson, R., Newport, R. J., and Smith, M. E.: The effect of zirconia content on the structure of zirconia-silica xerogels as determined by x-ray and neutron diffraction and Zr K-edge EXAFS and XANES, J. Phys.: Condens. Matter, 12, 3505–3519, https://doi.org/10.1088/0953-8984/12/15/301, 2000.

Muhich, C. and Steinfeld, A.: Principles of doping ceria for the solar thermochemical redox splitting of H_2O and CO_2, J. Mater. Chem. A, 5, 15578–15590, https://doi.org/10.1039/C7TA04000H, 2017.

Nakai, I., Akimoto, J., Imafuku, M., Miyawaki, R., Sugitani, Y., and Koto, K.: Characterization of the amorphous state in metamict silicates and niobates by EXAFS and XANES analyses, Phys. Chem. Miner., 15, 113–124, https://doi.org/10.1007/BF00308773, 1987.

Nasraoui, M., Bilal, E., and Gibert, R.: Fresh and weathered pyrochlore studies by Fourier transform infrared spectroscopy coupled with thermal analysis, Mineral. Mag., 63, 567–578, https://doi.org/10.1180/002646199548727, 1999.

Newville, M. and Ravel, B.: IFEFFIT and LARCH, in: X-ray absorption spectroscopy and related techniques, Vol. I, edited by: Chantler, C. T., Boscherini, F., and Bunker, B., https://doi.org/10.1107/S1574870720003407, 2020.

Oliveira, L. C. A., Ramalho, T. C., Souza, E. F., Gonçalves, M., Oliveira, D. Q. L., Pereira, M. C., and Fabris, J. D.: Catalytic properties of goethite prepared in the presence of Nb on oxidation reactions in water: Computational and experimental studies, Appl. Catal. B-Environ., 83, 169–176, https://doi.org/10.1016/j.apcatb.2008.01.038, 2008.

Omar, T. and Veiga, M. M.: Is niobium critical for Canada?, Extr. Ind. Soc., 8, 100898, https://doi.org/10.1016/j.exis.2021.100898, 2021.

Perrault, G.: La composition chimique et la structure cristalline du pyrochlore d'Oka, P.Q., Can. Mineral., 9, 383–402, 1968.

Piilonen, P. C., Farges, F., Linnen, R. L., Brown, G. E., Pawlak, M., and Pratt, A.: Structural Environment of Nb^{5+} in dry and fluid-rich (H_2O, F) silicate glasses: A combined XANES and EXAFS study, Can. Mineral., 44, 775–794, https://doi.org/10.2113/gscanmin.44.3.775, 2006.

Rudnick, R. L. and Gao, S.: Composition of the Continental Crust, in: Treatise on Geochemistry, edited by: Rudnick, R. L., 2nd Edn., Elsevier, 1–51, https://doi.org/10.1016/B978-0-08-095975-7.00301-6, 2014.

Shamblin, J., Feygenson, M., Neuefeind, J., Tracy, C. L., Zhang, F., Finkeldei, S., Bosbach, D., Zhou, H., Ewing, R. C., and Lang, M.: Probing disorder in isometric pyrochlore and related complex oxides, Nat. Mater., 15, 507–511, https://doi.org/10.1038/nmat4581, 2016.

Sheldrick, G. M.: SHELXT – Integrated space-group and crystal-structure determination, Acta Crystallogr. A, 71, 3–8, https://doi.org/10.1107/S2053273314026370, 2015.

Silveira, J. W. and Resende, M.: Competition in the international niobium market: A residual demand approach, Resour. Policy, 65, 101564, https://doi.org/10.1016/j.resourpol.2019.101564, 2020.

Siriya, P., Chanlek, N., Srepusharawoot, P., and Thongbai, P.: Excellent giant dielectric properties over wide temperatures of $(Al, Sc)^{3+}$ and Nb^{5+} doped TiO_2, Results Phys., 36, 105458, https://doi.org/10.1016/j.rinp.2022.105458, 2022.

Smith, M. P., Campbell, L. S., and Kynicky, J.: A review of the genesis of the world class Bayan Obo Fe–REE–Nb deposits, Inner Mongolia, China: Multistage processes and outstanding questions, Ore Geol. Rev., 64, 459–476, https://doi.org/10.1016/j.oregeorev.2014.03.007, 2015.

Subramanian, M. A., Aravamudan, G., and Subba Rao, G. V.: Oxide pyrochlores – A review, Prog. Solid. State Ch., 15, 55–143, https://doi.org/10.1016/0079-6786(83)90001-8, 1983.

Tarantino, S. C.: Mixing and ordering behavior in manganocolumbite-ferrocolumbite solid solution: A single-crystal X-ray diffraction study, Am. Mineral., 90, 1291–1300, https://doi.org/10.2138/am.2005.1641, 2005.

Thompson, R., Smith, P., Gibson, S., Mattey, D., and Dickin, A.: Ankerite carbonatite from Swartbooisdrif, Namibia: the first evidence for magmatic ferrocarbonatite, Contrib. Mineral. Petr., 143, 377–396, https://doi.org/10.1007/s00410-002-0350-0, 2002.

Tremblay, J., Bédard, L. P., and Matton, G.: Columbitization of fluorcalciopyrochlore by hydrothermalism at the Saint-Honoré alkaline complex, Québec (Canada): New insights on halite in carbonatites, Ore Geol. Rev., 91, 695–707, https://doi.org/10.1016/j.oregeorev.2017.08.027, 2017.

Wenger, M., Armbruster, T., and Geiger, C. A.: Cation distribution in partially ordered columbite from the Kings Mountain pegmatite, North Carolina, Am. Mineral., 76, 1897–1904, 1991.

Westre, T. E., Kennepohl, P., DeWitt, J. G., Hedman, B., Hodgson, K. O., and Solomon, E. I.: A Multiplet Analysis of Fe K-Edge 1s $\rightarrow$ 3d Pre-Edge Features of Iron Complexes, J. Am. Chem. Soc., 119, 6297–6314, 1997.

Wilke, M., Partzsch, G. M., Bernhardt, R., and Lattard, D.: Determination of the iron oxidation state in basaltic glasses using XANES at the K-edge, Chem. Geol., 220, 143–161, 2005.

Williams-Jones, A. E. and Vasyukova, O. V.: Niobium, Critical Metal, and Progeny of the Mantle, Econ. Geol., 118, 837–855, https://doi.org/10.5382/econgeo.4994, 2022.

Wong, J., Lytle, F. W., Messmer, R. P., and Maylotte, D. H.: K-edge absorption spectra of selected vanadium compounds, Phys. Rev. B, 30, 5596–5610, https://doi.org/10.1103/PhysRevB.30.5596, 1984.

Wu, B., Hu, Y.-Q., Bonnetti, C., Xu, C., Wang, R.-C., Zhang, Z.-S., Li, Z.-Y., and Yin, R.: Hydrothermal alteration of pyrochlore group minerals from the Miaoya carbonatite complex, central China and its implications for Nb mineralization, Ore Geol. Rev., 132, 104059, https://doi.org/10.1016/j.oregeorev.2021.104059, 2021.

Yamamoto, T.: Assignment of pre-edge peaks in K-edge x-ray absorption spectra of 3d transition metal compounds: electric dipole or quadrupole?, X-Ray Spectrom., 37, 572–584, https://doi.org/10.1002/xrs.1103, 2008.

Yang, H., Lu, R., Downs, R. T., and Costin, G.: Goethite, α-FeO(OH), from single-crystal data, Acta Crystallogr. E., 62, i250–i252, https://doi.org/10.1107/S1600536806047258, 2006.

Yong, T., Linnen, R. L., and McNeil, A. G.: An Experimental Study of Pyrochlore Solubility in Peralkaline Granitic Melts, Econ. Geol., 118, 209–223, https://doi.org/10.5382/econgeo.4958, 2022.

Yoshida, S., Tanaka, T., Hanada, T., Hiraiwa, T., Kanai, H., and Funabiki, T.: Analysis of XANES for identification of highly dispersed transition metal oxides on supports, Catal. Lett., 12, 277–285, https://doi.org/10.1007/BF00767210, 1992.

Zaitsev, A. N., Chakhmouradian, A. R., Siidra, O. I., Spratt, J., Williams, C. T., Stanley, C. J., Petrov, S. V., Britvin, S. N., and Polyakova, E. A.: Fluorine-, yttrium- and lanthanide-rich cerianite-(Ce) from carbonatitic rocks of the Kerimasi volcano and surrounding explosion craters, Gregory Rift, northern Tanzania, Mineral. Mag., 75, 2813–2822, https://doi.org/10.1180/minmag.2011.075.6.2813, 2011.

Zhang, Z., Middleburgh, S. C., de los Reyes, M., Lumpkin, G. R., Kennedy, B. J., Blanchard, P. E. R., Reynolds, E., and Jang, L.-Y.: Gradual Structural Evolution from Pyrochlore to Defect-Fluorite in $Y_2Sn_{2-x}Zr_xO_7$: Average vs Local Structure, J. Phys. Chem. C, 117, 26740–26749, https://doi.org/10.1021/jp408682r, 2013.